Photochemistry of 2-(2′-Hydroxyphenyl)benzothiazole Encapsulated in Nanosized Zeolites

S. Mintova,*,† V. De Waele,‡,§ M. Hölzl,† U. Schmidhammer,‡ B. Mihailova,† E. Riedle,*,‡ and T. Bein*,†

Department of Chemistry, LMU, Butenandtstrasse 11, 81377 Munich, Germany, Lehrstuhl für BioMolekulare Optik, LMU, Oettingenstrasse 67, 80538 Munich, Germany, and Laboratoire de Chimie Physique-UMR 8000, Université Paris Sud 11, Bat 349, 91405 Orsay, France

Received: May 14, 2004; In Final Form: August 31, 2004

The in situ incorporation and characterization of 2-(2′-hydroxyphenyl)benzothiazole (HBT) in the cages of nanosized FAU zeolites is reported. We demonstrate the advantage of using colloidal zeolite solutions to perform subpicosecond transient experiments on nanosized host/guest systems. FAU molecular sieve is prepared from precursor solutions containing as organic template only tetramethylammonium hydroxide (TMA) or both molecules HBT and TMA, using a hydrothermal treatment at 90 °C for 70 h. In situ dynamic light scattering investigations of the precursor solutions and the crystalline suspensions are performed with the original sample concentrations using a backscattering mode. The radius of the amorphous entities formed in the TMA-containing precursor solutions is about 25 nm, while that of the amorphous species in the HBT/TMA precursor solution is about 15 nm. The final particle size of FAU and HBT/FAU colloidal zeolites is 100 and 80 nm, respectively. The encapsulation of HBT with different concentrations into the large pore FAU molecular sieve host is confirmed by Raman, infrared, and ^{13}C solid-state NMR spectroscopies. The spectroscopic data reveal that the HBT molecules are incorporated in the nanosized zeolite particles, thus leading to changes in the environment of the TMA ions as well as in the local atomic arrangements of the FAU structure. At high concentration of HBT, a large fraction of the sodalite cages are destroyed, and the HBT and TMA molecules are located in the subsequently formed cavities. Steady-state UV−vis spectra also reveal the presence of the keto HBT-conformers inside the FAU zeolite nanocrystals. Upon UV excitation, the HBT molecules occluded in the zeolite nanoparticles undergo ultrafast intermolecular proton transfer within 1.5 ps.

Introduction

The versatile properties of molecular sieves have led to wide-ranging applications in fields such as catalysis, ion exchange, sensors, membranes, etc. Numerous new structures in which the molecular sieve materials have served as hosts for the supramolecular organization of ions, complexes, and clusters have been reported. Such structures are being used for the preparation of nonlinear optical systems, micro lasers, artificial antenna systems, photoinduced switches, information storage, pigments, etc.[1−5] The periodic system of well-defined cavities in zeolite-type crystals can maintain preferred orientations of organic guest molecules in the hosts, in contrast to amorphous solid-state materials in which the active centers are not regularly ordered.[6,7] For these applications, synthesis procedures for embedding different organic molecules such as azo dyes and spiropyrans have been established.[8−10] Widely investigated dyes were incorporated in molecular sieves such as zeolite Y, X, L, and $AlPO_4$-5.[11−18] The inclusion of dye molecules in the cavities of micro- as well as mesoporous materials that are stable toward extraction can be accomplished either via in situ ship-in-a-bottle synthesis or via covalent attachment on free silanol groups.

The synthesis of well-defined nanoscale zeolite crystals has been established in recent years. It has been shown that nanoscale amorphous gel particles are formed in the precursor solutions before long-range crystalline order is established. The chemistry of zeolite formation depends on many factors including the type of the initial precursor solutions, solubility of various species, aging time, crystallization temperature, time of heating, etc.[19−22] The ability to synthesize colloidal nanoparticles uniform in size, shape, composition, and bulk properties has played an important role in elucidating and understanding the optical behavior of some organic molecules incorporated in such materials. Moreover, colloidal molecular sieves can have high colloidal stability in different solvents with respect to further agglomeration and sedimentation. These features make the encapsulation of functional optical molecules in nanoscale zeolite suspensions an attractive synthetic target.

The compounds used to realize molecular devices undergo fast photochemical changes upon excitation with light. Their properties depend on the fast initial transformation that commonly takes place on the picosecond time scale or even faster. Complementary to the knowledge of the photoreactivity of the guest itself, investigating the molecular dynamics at the picosecond time scale provides information about the molecular motions in the zeolite and about the host/guest interactions. The investigation of intrazeolite photoreactivity has been the subject of a number of experimental studies, but the question of the molecular dynamics and reactivity on a picosecond time scale is slightly addressed. Up to now, most of the time-resolved

* Corresponding author. Phone: +4989 21807625. Fax: +4989 21807622. E-mail: svetlana.mintova@cup.uni-muenchen.de.
† Department of Chemistry, LMU.
‡ Department of Biomolecular Optics, LMU.
§ Université Paris Sud 11.

10.1021/jp047924j CCC: $27.50
Published on Web 11/09/2004

TABLE 1: Chemical Compositions of the Initial Precursor Mixtures Used for Preparation of FAU and HBT/FAU Samples

samples	HBT	$(TMA)_2O$	Al_2O_3	SiO_2	H_2O	EtOH	HBT/$(TMA)_2O$
FAU		2.1	1.0	4.3	136	15	0
HBT/FAU-1	3.8×10^{-3}	2.1	1.0	4.3	136	15	0.0018
HBT/FAU-2	5.1×10^{-3}	2.1	1.0	4.3	136	15	0.0024
HBT/FAU-3	7.4×10^{-3}	2.1	1.0	4.3	136	15	0.0035
HBT/FAU-4	8.0×10^{-3}	2.1	1.0	4.3	136	15	0.0038
HBT/FAU-5	7.4×10^{-2}	2.1	1.0	4.3	136	15	0.035

measurements on zeolites were performed using diffuse reflectance on powder samples.[23−25] This technique demands a precise methodology in the data acquisition and a careful treatment to obtain quantitative results. In particular, the nonhomogeneity of the samples and the related parameters such as particles size, packing, and light penetration depth are factors that obscure the experiments in the subnanosecond regime. One strategy for investigation of intrazeolite photochemistry on the picosecond time scale involves application of transmission spectroscopy. This approach has been successfully applied using IR domains, where zeolites are transparent and nonscattering.[26,27] One other alternative involves using single monocristals instead of powder samples. Picosecond fluorescence[28] and pump−probe transient absorption[29] measurements in the visible range were performed. However, the use of monocrystals for pump−probe experiments is limited to the study of molecules that undergo reversible photo transformation due to the fact that the samples cannot be refreshed during the measurements. In a recent paper, Castagnola and Dutta[30] proposed an interesting alternative for investigating fast chemical processes using colloidal suspensions of nanosized zeolites. We extend further the concept toward ultrafast photochemical processes on the femtosecond time scale in zeolite suspensions. As probe molecule, we consider HBT for the reasons described next.

The photophysical and photochemical properties of HBT have been investigated extensively,[31−42] due to an ultrafast excited-state proton transfer that takes place in less than a few picoseconds. The photophysical properties of this compound depend strongly on the molecular surroundings. The photoreactivity is mainly governed by the existence of intramolecular hydrogen bonds between the OH group and the close N atom. Upon UV excitation, the molecules undergo a very fast excited-state intramolecular proton transfer (ESIPT) in aprotic solvents. In the presence of solvent with proton acceptor or donator groups, the intramolecular hydrogen bond of HBT breaks, thus changing the photochemical behavior of HBT. The high sensitivity of the HBT molecules to their surrounding renders them as interesting probes for the specific local atomic environment in the zeolite hosts. In addition, they are promising candidates as guests in functionalized zeolite hosts for applications such as UV filtering, sensing, and molecular switching.[42]

In the first part of the article, we describe the in situ incorporation of 2-(2′-hydroxyphenyl)benzothiazole (HBT) inside the supercages of nanosized FAU zeolite from a precursor colloidal solution via hydrothermal treatment at conditions typical of colloidal systems. The evolution of FAU nanoparticles synthesized with and without addition of HBT is monitored by in situ dynamic light scattering in backscattering mode as a function of the crystallization time and the degree of HBT-loading. The resulting crystalline zeolite nanoparticles were characterized by ^{13}C NMR, Raman, and IR spectroscopies. In the second part, we focus on the photophysical and chemical properties of HBT occluded in the supercages of FAU-type particles. The steady-state UV−vis spectroscopic properties of HBT incorporated in FAU nanocrystals were compared to HBT dissolved in ethanol and water. Finally, the time-resolved behavior of HBT/FAU samples is examined.

Experimental Procedures

Synthesis of Nanosized Zeolite Crystals. Nanosized pure FAU and HBT/FAU crystals containing only TMA and both TMA and HBT, respectively, were prepared from clear precursor solutions with the following molar compositions:

FAU:2.1 $(TMA)_2O$:1.0 Al_2O_3:4.3 SiO_2:136 H_2O and

HBT/FAU:*x* HBT:*y* $(TMA)_2O$:1.0 Al_2O_3:4.3 SiO_2:136 H_2O:*z* EtOH.

The starting mixture for the pure FAU sample was formed by mixing tetramethylammonium hydroxide pentahydrate ($TMAOH{\cdot}5H_2O$), aluminum isopropoxide (98%), and silica sol (30 wt. %, particle size ∼5 nm) with doubly distilled water. The resulting mixtures were vigorously stirred for 1 h to obtain clear solutions. Starting mixtures for HBT/FAU samples containing different amounts of 2-(2′-hydroxyphenyl)benzothiazole were prepared from the previous compounds, and finally, commercially available HBT dissolved in ethanol was added. The molar ratios between different compounds for all FAU and HBT/FAU samples are summarized in Table 1. The previous precursor solutions were further stirred for about 60 min at room temperature (RT) and then aged on an orbital shaker for 24 h prior to the subsequent crystallization at 90 °C. The nanosized FAU crystals resulting from this hydrothermal (HT) treatment were purified via separation from the mother liquor by three steps of centrifugation (20 000 rpm, 60 min). After each step, the nanoparticles were redispersed in ethanol (98%) or in doubly distilled water using an ultrasonic bath for 3 h.

Characterization of Colloidal Solutions Containing Nanosized Zeolite Crystals. In situ dynamic light scattering (DLS) was applied to investigate the particle size distribution in concentrated aqueous solutions of TMA, HBT, SiO_2, and Al_2O_3 at room temperature and during a HT treatment at 90 °C. The measurements were performed with ALV-NIBS/HPPS DLS in backscattering geometry (scattering angle 173°), using an HeNe laser operating at 632.8 nm wavelength and with an output power of 3 mW. The typical measurement settings included 60 scans, and the calculated polydispersity index, i_p, was used to obtain a multimodal particle size distribution. For the cases with $i_p > 0.2$, the results from the cumulant analysis were neglected, and only the data from the distribution function analysis (DFA) were taken into account. The Rayleigh−Debye model was used for the DFA calculations. The results are displayed as an unweighted particle size distribution, which shows the scattered intensity per particle size classes.

Prior to further investigations, the samples were purified by centrifugation, frozen in liquid nitrogen, and dried in a Christ Alpha 1-4 vacuum freeze-drier overnight. Powder X-ray diffraction (XRD) data were collected on a Scintag XDS 2000 (liquid N_2 cooled Ge detector, CuK_α radiation, $\theta-\theta$ geometry). The infrared (IR) transmittance and the Raman scattering data were recorded with a Bruker Equinox 55 FT-IR spectrometer. The Raman measurements were performed using an FRA106/S

FT-Raman module, an Nd:YAG laser (1064 nm excitation light), and a liquid N_2 cooled Ge detector. Scanning electron microscopy (SEM) images were recorded using a Philips XL 40 microscope. The solid-state ^{13}C magic-angle spinning nuclear-magnetic resonance (MAS NMR) spectroscopic experiments were carried out with 4 mm ZrO_2 rotors in a commercial double resonance probe using a Bruker DSX avance 500 spectrometer.

The steady-state absorption in the ethanolic and water solutions of HBT/FAU samples was measured with a Specord S100 spectrometer from Analytik Jena. The steady-state emission spectra were recorded with a fluorescence spectrometer type Spex-Fluorolog-2.

Time-resolved measurements were performed using a pump−probe setup generated from 150 fs pulses at 772 nm and delivered at 1 kHz by an amplified Ti:sapphire laser system (Clark-MXR CPA 2001). The pump at 386 nm is generated in a 300-μm BBO crystal by frequency doubling. As a probe, we use a supercontinuum generated by focusing a few microjoules of the 772 nm pulses into a sapphire plate (2 mm thickness). The fluctuations of the continuum are compensated using a reference beam. The pump and the probe are focused by an off-axis parabolic mirror. The beams from the probe and from the reference are dispersed in a monochromator and detected with photodiodes (Becker & Hickel PDI-400-1-P-UV). The dispersion of the supercontinuum was minimized by using nondispersive optics along the optical path and by the use of a 200 μm window at the front of the cell. The pump energy was limited to about 250 nJ per pulse to avoid nonlinear effects as triple photoionization of water. All colloidal zeolite suspensions were measured using flowing cell with an optical path of 1 mm. The time-resolution of the setup determined for the zeolite suspensions and for the pure solvent was found to be higher than 300 fs, the limitation coming from the optical path, not from the size of the zeolite nanoparticles (for details, see the following discussion).

Results and Discussion

Crystal Growth of Nanosized Zeolites: in Situ DLS and XRD Investigations. Clear precursor solutions for pure FAU and HBT/FAU samples were prepared as described previously and after 24 h of aging at RT were transferred into a fused silica cuvette and subjected to in situ DLS measurements. A major advantage of the in situ study is the elimination of invasive procedures that may modify the crystallization process of the FAU zeolite. The backscattering of light produced from the X-ray amorphous sample was strong enough to be monitored as a function of the particles existing in the water-clear precursor mixtures. The mean particle radius (r) is calculated according to the equation $r = k_BT/6\pi\eta D$, where k_B is the Boltzmann constant, T is the actual temperature of the dispersion, η is the solvent viscosity, and D is the diffusion coefficient. For FAU and HBT/FAU-1 samples, the mean radius increases from 25 to 100 nm and from 15 to 80 nm, respectively, when the heating time is increased from 20 to 70 h. The polydispersity index also increases with increasing the heating time, suggesting a multimodal particle size distribution in these samples as a function of the crystallization time. The value of the polydispersity index is significantly larger than 0.2; therefore, the calculated mean hydrodynamic radius is not longer reliable, and independent distribution function analyses were carried out for these samples. Figure 1 shows the DFA data of the samples FAU, HBT/FAU-1, and HBT/FAU-3 heated in the in situ quartz cell of the DLS instrument. As can be seen, colloidal particles with a size of about 15−25 nm were detected for all samples

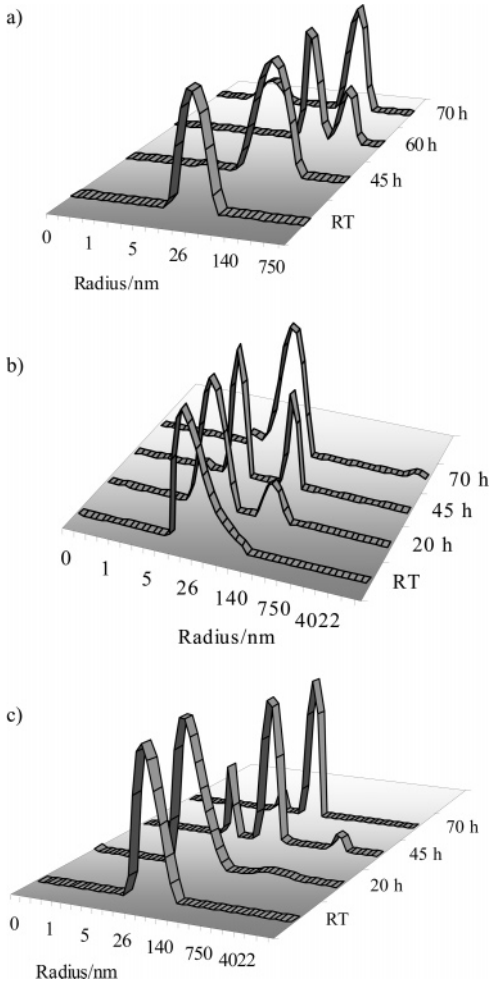

Figure 1. DLS data of (a) FAU, (b) HBT/FAU-1, and (c) HBT/FAU-3 precursor solutions aged at room temperature for 24 h and subjected to hydrothermal treatment at 90 °C up to 70 h. The DFA is displayed as scattering intensity per unweighted particle size classes.

aged at RT. These particles correspond to the amorphous entities formed immediately after mixing of all compounds. Prior to heating, all the colloidal particles were shown to be amorphous by X-ray diffraction. After a prolonged time of heating of solution FAU (about 60 h), two particle populations are observed (Figure 1a). When increasing the heating time to 70 h, the peak corresponding to particles with a larger size becomes very pronounced, and the width of the particle size distribution curves becomes narrow (Figure 1a). According to the XRD data, the solid phase extracted from this precursor solution is entirely crystalline, and all Bragg reflections typical of the FAU structure are observed (see Figure 2a). In the samples HBT/FAU-1 and HBT/FAU-3 loaded with different amounts of HBT, an increase of the scattering intensity due to the presence of a second generation of particles with radius of about 50−90 nm is observed after 20 and 45 h HT treatment, respectively (Figure 1b,c). The formation of colloidal entities with small hydrodynamic radius (∼15 nm) in sample FAU/HBT-1 leads to the formation of small FAU nanocrystals after 70 h HT treatment (Figure 1b). The corresponding evolution of the light scattering data suggests that the zeolite phase is represented by the radius fraction at about 80−100 nm, while the smaller-size fractions are still amorphous. On the other hand, the formation of larger primary particles in sample FAU/HBT-3 results in larger FAU crystals (∼140 nm) when more HBT was employed (Table 1). The XRD patterns of the samples heated for 70 h demonstrate the existence of fully crystalline FAU material from solutions

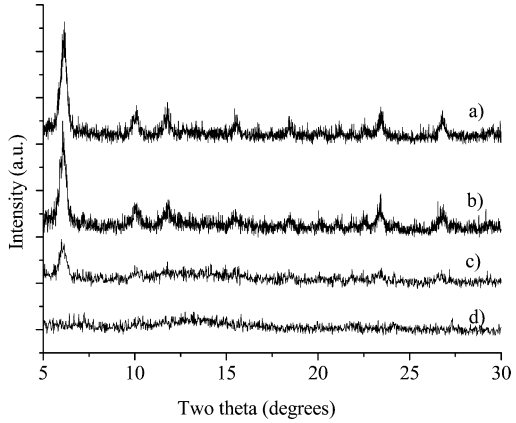

Figure 2. Powder diffraction patterns of samples (a) FAU, (b) HBT/FAU-1, (c) HBT/ FAU-4, and (d) HBT/FAU-5 after hydrothermal treatment at 90 °C for 70 h. The XRD pattern of HBT/FAU-2 and HBT/FAU-3 resembles that of HBT/FAU-1 (patterns are not shown).

HBT/FAU-1, -2, and -3, while HBT/FAU-4 contains some amorphous phase that is visible in the XRD patterns (Figure 2). The purified and freeze-dried samples obtained from solution FAU/HBT-5 exhibit no Bragg reflections (Figure 2d). The particle radius of the FAU and HBT/FAU samples determined by SEM is in a good accordance with the DLS data.

Nanosized Zeolites: Spectroscopic Investigation. A Raman spectroscopic investigation was carried out to study the manner of incorporation of HBT in the nanosized FAU samples. Figure 3 shows the Raman spectra below 1800 cm^{-1} of a series of HBT/FAU samples with different ratios of HBT/TMA^+ molecules (see Table 1). The relatively low concentration of HBT hampered to distinguish unambiguously the Raman signals generated by HBT. Although, in the spectrum of sample HBT/FAU-4, one observes resolved Raman scattering near 1600 cm^{-1}, which is typical of aromatic vibrations. As seen in Figure 3a, HBT generates a very intense Raman peak near this wavenumber, while TMA does not produce any signal. In addition, monotonic changes in the spectral signature of FAU with the increase of the HBT concentration are detected, thus giving indirect evidences for embedding of the dye molecules in the zeolite structure. The most pronounced changes in the spectral profile upon adding different amounts of HBT appear between 250 and 550 cm^{-1} and in the band near 760 cm^{-1}. The latter originates from the symmetrical C−N stretching mode of TMA existing in the zeolite particles. The Raman signal at 760 cm^{-1} shifts to about 771 cm^{-1} or to about 753 cm^{-1}, depending on whether the TMA ions are trapped in the sodalite cages (β-cages) or in the supercages (α-cages), respectively.[43,44] The higher position of the Raman peak for the TMA occluded in the sodalite cages results from the tight fit of the cation size (∼6.4 Å) to the cage size (∼6.8 Å), which leads to a strong elastic stress of the TMA ions along the C−N bond directions. Hence, on the basis of the integrated intensities (I) of the peaks at 753 and 771 cm^{-1}, one can define a quantitative measure of the relative amount of TMA occluded in the sodalite cages via the ratio $I_{771}/(I_{753} + I_{771})$. As can be seen in Figure 3b, the incorporation of HBT into the zeolitic structure decreases monotonically the amount of TMA ions placed in sodalite cages. This may be due to two reasons: (i) the presence of HBT forces the TMA ions to fill predominantly the super-cages and (ii) the sodalite-type structural units are partially destroyed due to the impact of the large HBT molecules trapped in the structure. On the other hand, the aluminosilicate materials built of sodalite blocks are characterized by a sharp and very intense Raman peak near 500 cm^{-1}.[44−47] In the pure FAU sample, this peak

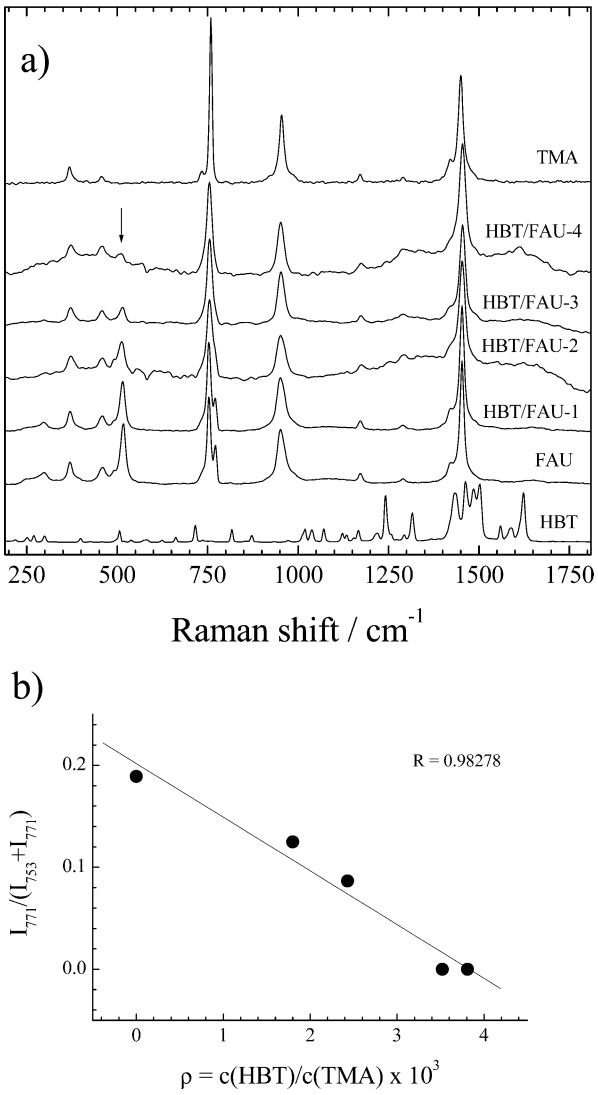

Figure 3. (a) Raman spectra of HBT/FAU samples prepared with different ratios between HBT and TMA. The spectra of pure TMA·$5H_2O$ and HBT are given as references. The arrow marks the position of the most intense Raman peak originating from the skeleton atom vibrations in FAU-type zeolite. The spectra are normalized to the integrated intensity of the Raman scattering band between 700 and 800 cm^{-1}, which arises from the symmetrical C−N stretching of TMA. (b) Relative amount of TMA ions located in the sodalite cage (represented via the relative integrated intensity of the peak at 771 cm^{-1}) vs the ratio between HBT and TMA occluded in the inorganic matrix; the integrated intensities are obtained after fitting the spectrum profile with Lorentzians. The experimental values can be linearly fitted with a correlation coefficient of $R = 0.98$ and a standard deviation of SD = 0.017.

appears at 516 cm^{-1} (see Figure 3a). The presence of HBT incorporated together with TMA in the HBT/FAU samples leads to a decrease in the intensity of this peak, thus pointing to a partial destruction of the sodalite structural units. Therefore, the main reason for the disappearance of sodalite-cage-placed TMA is the existence of local structural disorder in the T−O network. However, the sodalite unit peak is still present in the Raman spectra of samples with a high amount of HBT (HBT/FAU-3 and HBT/FAU-4), although no TMA occluded in sodalite cages is observed (Figure 3a). The spectral data suggest that the HBT molecules interact with the neighboring TMA cations and for high degrees of HBT-loading, HBT−TMA complexes may be formed. The formation of a complex of TMA−HBT is supported by the appearance of an additional peak at 2852 cm^{-1} in the

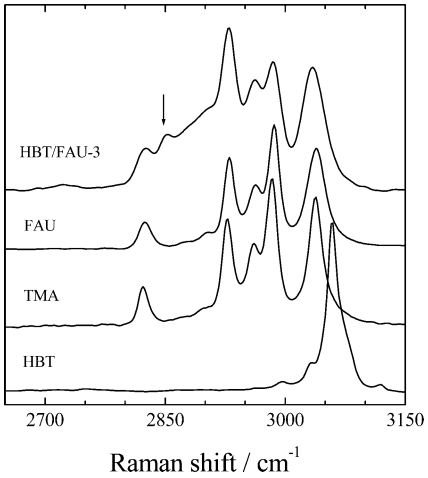

Figure 4. High-wavenumber Raman spectra of pure TMA·5H_2O, HBT, FAU, and HBT/FAU-3 samples.

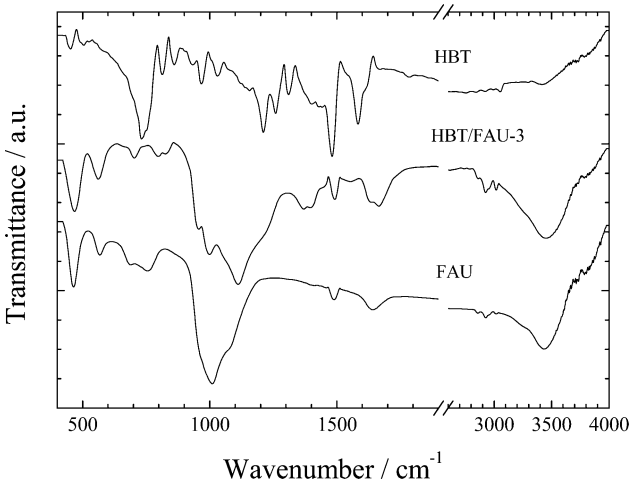

Figure 5. IR spectra of HBT, pure FAU, and HBT/FAU-3 sample.

spectra of samples with high amount of HBT (see Figure 4). The extra peak is positioned in the range of C−H stretching vibrations and most probably results from perturbed C−H bonds of TMA that are involved in atomic interactions with the HBT molecules. Occurrence of a large size organic complex will affect the inorganic network by breaking some T−O−T linkages and damaging the highly symmetric sodalite-type structural blocks. Indeed, partial amorphization of sample HBT/FAU-4 is deduced from the increase in the Raman scattering between 300 and 500 cm^{-1}, which is typical of noncrystalline silica and alumosilicates.[48] The IR transmittance data also reveal a strong change in the T−O systems when the HBT molecule is embedded in the zeolitic structure (see Figure 5). The IR absorption between 650 and 850 cm^{-1} is sensitive to the mutual orientation of TO_4 units in silica and alumosilica type materials.[49] The difference in this spectral range between pure FAU and HBT/FAU-3 samples also indicates that intertetrahedral rearrangements take place when HBT molecules are trapped in the structure. In addition, the most intense absorption band centered near 1015 cm^{-1}, which originates from the Si−O bond stretching modes, shifts to higher energies, thus pointing to a stiffness of the Si−O bonds due to the presence of HBT as a cotemplate in addition to the structure directing agent (i.e., TMA for FAU structure). The Raman and IR data reveal the change in the TMA^+ surroundings when FAU is synthesized in the presence of HBT and show the occurrence and a systematic increase in the structural disorder in FAU skeleton upon adding HBT.

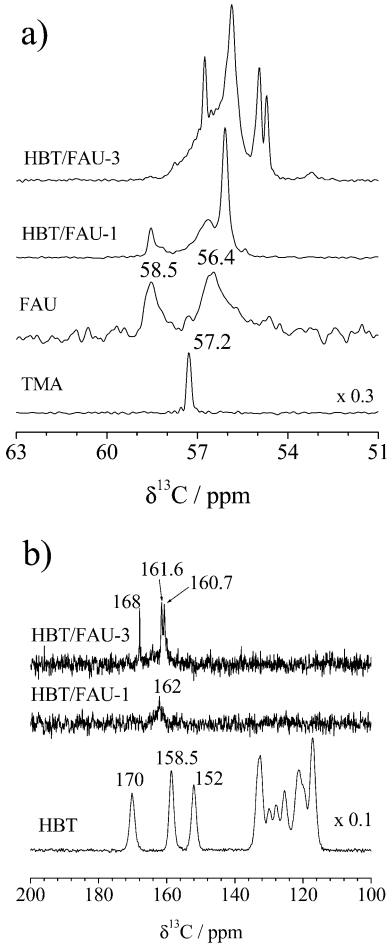

Figure 6. NMR spectra of pure TMA·5H_2O, FAU, and samples HBT/FAU-1 and HBT/FAU-3 in the range of (a) 50−63 ppm and (b) 100−200 ppm.

A solid-state ^{13}C NMR spectroscopic study was performed to clarify the presence of HBT in the host−guest systems. The ^{13}C NMR spectra of samples HBT/ FAU-1 and -3 are compared with pure FAU, TMA, and HBT samples (Figure 6 a,b). In the ^{13}C NMR spectrum of pure TMA, only one shift at 57.2 ppm is observed (Figure 6a). For the FAU sample, this peak splits in two (i.e., at 58.5 and 56.4 ppm). According to a previous investigation of ZK4-type zeolite synthesized from TMA-containing gel, a signal at 58.8 ppm is related to TMA located in the β-type cages, while a signal at 56.9 ppm corresponds to TMA placed in the larger alpha cages.[50] Analogically, we assign the 58.5 ppm signal to TMA ions embedded in the sodalite cages of FAU structure and that at 56.4 ppm to TMA in the supercages of FAU zeolite. Thus, the NMR data, similarly to the Raman data, demonstrate the existence of two types of TMA species differing from each other in their location in the FAU structure. With increasing the degree of HBT-loading from HBT/FAU-1 to HBT/FAU-3 samples, the signal at 58.5 disappears, and more peaks are observed in the spectral range of 50−60 ppm (see Figure 6a). The former result points to the loss of tightly embedded TMA in the structure, while the latter suggests additional changes in the environment of the C atoms of the TMA molecules. The NMR data confirm the interpretation of the Raman and IR data regarding: (i) the initial modification in the surroundings of TMA due to the different locations in the host structure and (ii) the disappearance of TMA trapped in the sodalite-type cages with an increase of HBT in the FAU structure. ^{13}C chemical shifts for pure HBT are observed between 180 and 100 ppm (see Figure 6b). Pure FAU containing

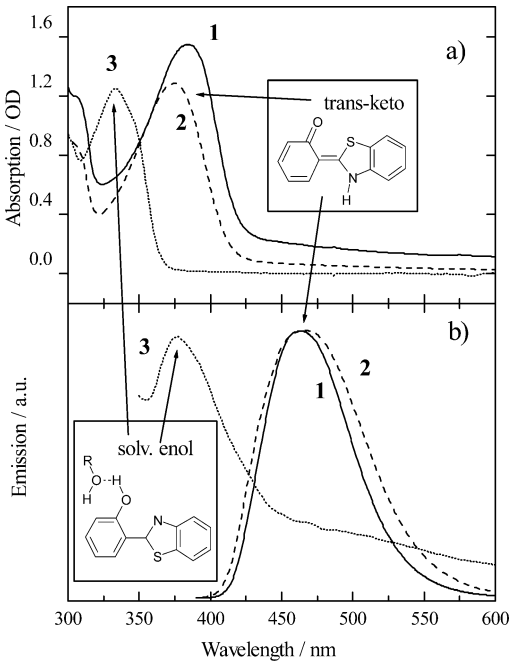

Figure 7. (a) Absorption spectra of HBT/FAU-1 (line 1, measured in 1 cm cell) and HBT/FAU-3 (line 2, measured in 1 mm cell). The absorption of HBT dissolved in EtOH is also given for comparison (line 3). (b) Normalized emission spectra of HBT/FAU-1 (line 1), HBT/FAU-3 (line 2), and HBT in ethanol (line 3) excited at 380 nm.

only TMA molecules does not produce any signal in this spectral region. Thus, additional peaks appearing upon HBT-loading should be related to the HBT molecule incorporated in the zeolite structure. It is worth noting that due to the strong influence of the surroundings (TMA^+, framework acidic sites), the ^{13}C NMR features of the HBT guest may differ substantially from those of pure HBT. In the range 180−100 ppm, a weak and broad peak at about 162 ppm is detected for sample HBT/FAU-1 (Figure 6b). NMR signal near 155 ppm is typical for carbon bonded to oxygen atom in phenol.[51] The additional chemical shift of this peak may be due to interactions between a methyl group of TMA and the phenol group of HBT.[52] The latter assumption corresponds well with the appearance of an additional ^{13}C NMR signal at 56.0 ppm related to the carbon nuclei of TMA. For sample HBT/FAU-3, more additional signals are observed in the ranges 170−150 ppm and 59−53 ppm, generated by HBT and TMA, respectively, which points to amplification of the mutual influence of TMA and HBT upon HBT-loading. The deviations in the chemical shift and the change in the relative intensities suggest that the HBT molecules behave as entities embedded in a solid-state host matrix (i.e., that HBT is incorporated in the bulk of the FAU-type nanoparticles).

Steady-State UV−vis Spectroscopy. The absorption and the emission spectra of samples HBT/FAU-1 and HBT/ FAU-3 are depicted in Figure 7. The spectra of pure HBT dissolved in ethanol are also given for comparison. As can be seen, the conformation of HBT in HBT/FAU samples is not the enol-form observed for HBT in ethanol.[35,36,39] The nature of the species responsible for the absorption at about 380 nm is described in the literature.[35,36,39,40,41] Some authors assign the absorption band to the deprotonated HBT anion, others to the keto-tautomer. The emission was without any doubt identified as coming from the deprotonated HBT molecules.[35,40,41]

The incorporated HBT molecules in zeolite nanoparticles change their microenvironment in a different way as compared to that already observed in solutions. By comparing the absorption and emission of the samples HBT/FAU-1 and HBT/FAU-3, a significant shift of the maximum of absorption of HBT between the two samples is observed. In sample HBT/FAU-1, the peak maximum is at 385 nm, while it is blue-shifted to 375 nm in sample HBT/FAU-3 (Figure 7a). In comparison, the shift of the emission band is negligible (see Figure 7b). If emission and absorption involve the same minimum of the S_1 potential energy, then the $S_1 \rightarrow S_0$ and $S_0 \rightarrow S_1$ spectra will have the same but mirror appearance. Such case for HBT molecules dissolved in ethanol is observed (see Figure 7). The decoupling of absorption and emission in HBT/FAU samples clearly reveal the distinct nature of the emissive and absorbing state; thus, we assign the absorption to the keto HBT tautomer and the emission to the anion. To summarize, the HBT ground-state conformation results from an enol−keto equilibrium, which in this case is catalyzed by the high alkalinity of the initial solution. In neutral solution, the enol form is the stable one. In our solutions, the pH is higher than 10; therefore, we observe the solvent-assisted formation of the keto conformer. The keto conformer is also the stable form of HBT molecules incorporated in HBT/FAU samples.

An estimation of the HBT-loading in the sample HBT/FAU-3 can be deduced from the absorption spectrum. Under the assumption that the extinction coefficient of HBT−keto does not differ strongly from the one of HBT−enol ($\epsilon_{max} = 20\,000$ mol^{-1} cm^{-1}), the concentration of HBT in the sample HBT/FAU-3 is about 0.7 mM. Considering that the solid concentration of zeolite particles in the colloidal suspension is about 1 wt %, we estimate that the concentration of HBT in the supercages of FAU sample is about 5 mM. This corresponds to loading of one HBT molecule per unit cell, or about 1 HBT molecule for eight supercages. Therefore, for such a degree of HBT loading, there is a small probability for a direct interaction between two HBT molecules. However, since one supercage is surrounded by six sodalite cages, the amount of HBT is certainly sufficient to induce a redistribution of the H_2O or TMA^+ molecules as observed in the Raman and NMR spectra of HBT/FAU samples. The presence of neighboring HBT and TMA^+ in the same cavity, as already suggested from the analysis of the Raman and NMR spectra, might also explain the blue shift of the HBT absorption band. Complementary studies are, however, necessary to clarify the interactions between the molecules of HBT and TMA^+ and a spatial constraint of both molecules confined in the same supercage.

Picosecond Dynamics of HBT Molecule Encapsulated in Nanoscale Zeolite Crystals. We measured the transient spectra of HBT in FAU for several pump−probe delays in the range 1−50 ps following the subpicosecond excitation at 386 nm. Figure 8 shows typical transient spectra recorded for HBT/FAU-3 in the range of 1−5 ps (a) and 5−50 ps (b). The transient signal recorded for pure FAU colloidal suspension is also given in Figure 8a. As can be seen, the nanocrystalline suspension exhibits no transient absorption signal when excited at 386 nm. Therefore, under the experimental conditions used, the solvated electron, which is characterized by a broad absorption band centered at 730 nm in aqueous solution, is not formed in the colloidal suspension by multiphoton absorption of the pump pulse. Hence, the transient spectra recorded in HBT/FAU-3 can unambiguously be attributed to the HBT molecules embedded in FAU. They exhibit a strong stimulated emission band with a maximum around 480 nm and a broad transient absorption centered at 710 nm. A second absorption band peaks in the near-UV border of our spectral window. The transient is formed in less than 1 ps and evolves slightly in shape on the 1−50 ps

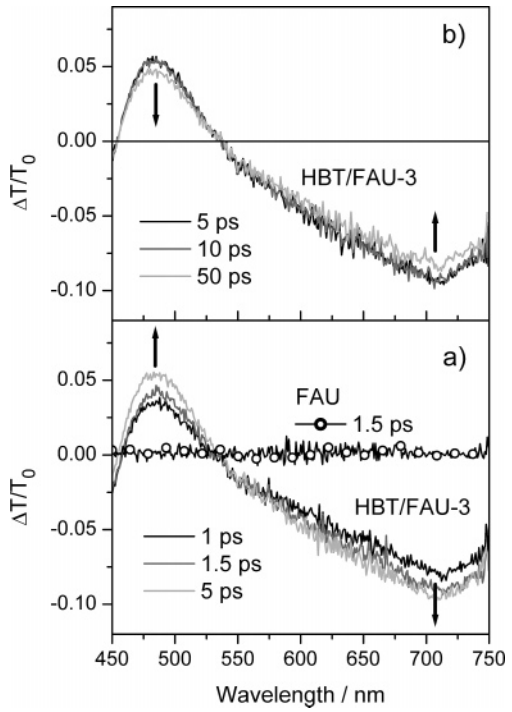

Figure 8. Transient transmission spectra of sample HBT/FAU-3 after excitation at 386 nm: (a) from 1 to 5 ps and (b) from 5 to 50 ps. The arrows mark the direction of the signal evolution. The transient signal after excitation at 386 nm of the pure FAU zeolite suspension without HBT is given for comparison (a).

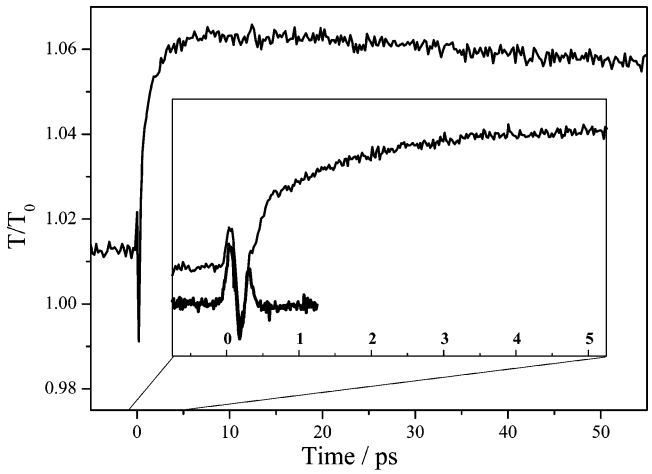

Figure 9. Transient transmission change of sample HBT/FAU-3 recorded at 480 nm after excitation at 386 nm. The signal from pure water is also given for comparison.

time scale. During the first picosecond, an increase of the stimulated emission band together with an increase of the absorption band in the near-IR is observed. Within the first 5 ps, the emission band shifts slightly to higher energies (from 485 to 482 nm). After 5 ps, the spectra do not change anymore in shape, but their intensity decreases within hundreds of picoseconds (Figure 8b). The parallel time behavior of the stimulated emission band and absorption band suggests that the same transient species is responsible for the emission and for the absorption.

Additionally, the kinetics of the stimulated emission band in HBT/FAU-3 has been measured at $\lambda_{probe} = 480$ nm for a pump−probe delay varying from −5 to +50 ps (Figure 9). The signal can properly be fitted by a sum of three exponential decays: the first time constant $\tau_1 = 0.15$ ps corresponds to the excited-state population created during the pump excitation, the second time constant reflects the increase of the stimulated emission band with $\tau_2 = 1.5$ ps, and finally, the stimulated emission disappears with $\tau_3 = 350$ ps. One should note that the accuracy of the last decay is somehow uncertain considering the pump−probe delay scanned in our experiment. Precise determination of τ_3 requires measurements on nanosecond time scales, which will be a subject of a following paper. However, the time of disappearance of the stimulated emission band, τ_3, is clearly longer than the usual decay of the S_1 keto tautomer that has been measured to be around 100 ps at room temperature (see ref 33 and references therein). In the literature, this fast decay of the HBT keto tautomer is related to a very efficient $S_1 \rightarrow S_0$ internal conversion process governed by a conical intersection, which is responsible for the photostability of the compound. The second time $\tau_2 = 1.5$ ps is also unusual for the photochemistry of HBT. It is indeed much slower than the common time of intramolecular excited-state proton transfer (about 100 fs or faster).

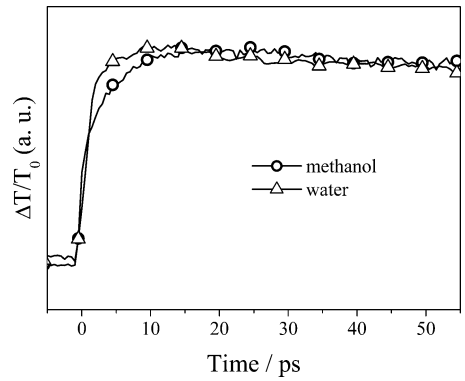

Figure 10. Transient transmission change of alkaline solution of HBT in water and methanol recorded at 480 nm after excitation at 386 nm.

To clarify the confinement effects on the picosecond dynamics of HBT encapsulated in the zeolite cavities, we performed complementary measurements in solution. As described previously, the stationary spectrophotometric data on HBT/FAU samples indicate the presence of a keto-like conformer into the nanocrystals of zeolite. While the ESIPT of HBT has been extensively studied, the photoinduced reactivity of the HBT-keto tautomer has not been reported in the literature. We stabilized a keto-like tautomer of HBT in aqueous and alcoholic solution under alkaline condition (pH >12) and followed the photoinduced picosecond dynamics after excitation at 386 nm under the same conditions as for the HBT/FAU samples. We obtained similar transient spectra for the HBT-keto in water and in methanol as those measured for HBT/FAU. The kinetics at 480 nm was measured for both alkaline solutions (Figure 10). The global time evolution of the signal for both solutions is similar to that recorded for HBT/FAU. The stimulated emission is partially formed during the pump pulse duration. It increases during a few picoseconds and then decays slowly within hundreds of picoseconds. We reproduced the two decays with the same exponential fit function as that used for HBT/FAU and found that τ_2 equals 1.6 and 4.4 ps for water and methanol, respectively, and τ_3 equals 500 ps for both samples (likewise, HBT/FAU τ_1 was fixed to 0.15 ps to reproduce the pump duration). The similarity of the kinetics behavior in solution and FAU system reveals that the picosecond dynamics of HBT is not directly modified when the molecule is occluded into the zeolite cavities. It is worth noting that the first decay time is the same in water and zeolite, while it is about three times slower in methanol, thus suggesting that the decay is

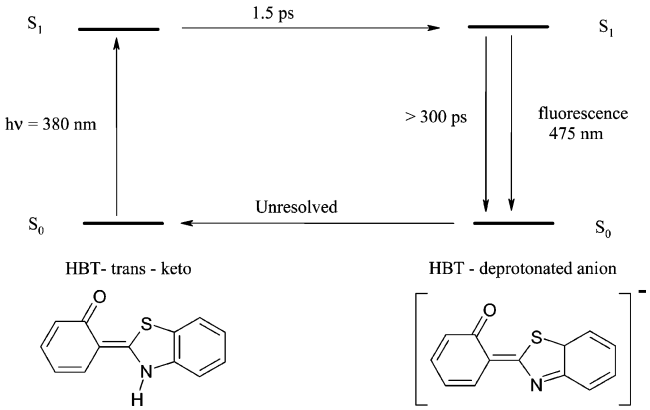

Figure 11. Deprotonation mechanism of HBT in FAU.

governed by the first solvation shell surrounding the HBT molecule. On the basis of steady-state UV−vis, we have previously demonstrated that the absorption band around 380 nm is assigned to the keto tautomer,[36] while the emission is due to the deprotonated anion.[35] The assignment of these bands was reinforced by the kinetics of the stimulated band. It is known that the deprotonated anion has a much slower decay time than the keto tautomer of HBT.[35] Recently, this general property of ESIPT molecules has also been investigated theoretically.[53] We assign therefore the fast picosecond decay to the deprotonation time of HBT-keto to form the HBT deprotonated anion. Such time constants have been reported for excited-state deprotonation.[54] The slower decay is very close for both alkaline solutions and appears faster in zeolite, but in the same order of magnitude. As aforementioned, our experimental setup is not well-adapted for investigating dynamics on the nanosecond time scale; the values for this slower decay should be taken carefully. However, the internal conversion from the excited anion proceed via structural reorganization of HBT. Hence, it would not be surprising to observe effects of the confinement in the zeolite cage on this time decay. The deprotonation mechanism of HBT in FAU structure is depicted in Figure 11.

In addition to the photochemistry of HBT, it is important to estimate the time-resolution accuracy of the set up and to verify that the nanosized particles in the zeolite suspensions do not impact on the sensitivity of the measurements. This is confirmed by comparing the width of the coherent artifact in pure water with the coherent artifact in sample HBT/FAU-3. In this case, the artifact results from nonlinear interaction between the pump and the probe beam.[55] It takes place only during the temporal overlap of the probe and pump pulses, and therefore, reflects the temporal resolution of the setup. As can be seen in the insert of Figure 9, the coherent artifact is exactly the same for pure water and for sample HBT/FAU-3. Moreover, the zeolite nanoparticles are transparent in the visible and near-UV range, and no photoreactivity can be triggered at 386 nm (see Figure 8).

Conclusions

2-(2′Hydroxyphenyl)benzothiazole molecules were successfully incorporated into the voids of nanosized FAU type zeolite through a hydrothermal treatment of colloidal precursor solutions in the presence of the structural directing agent TMA and HBT as a cotemplate. A DLS study reveals that the aged precursor solutions contain particles with a hydrodynamic radius of ∼25 and ∼15 nm for pure FAU and HBT/FAU samples, respectively. The initially formed nanoparticles are amorphous according to the XRD data, and they are transformed into FAU-type nanocrystals of size 80−100 nm under heating at 90 °C for 70 h. Raman, infrared, and solid-state ^{13}C NMR spectroscopic studies demonstrate that the embedding of the HBT molecules changes the local structure of the FAU skeleton, destroying partially the sodalite-type cages, and affects the atomic surroundings of the TMA ions. For high degrees of HBT loading, the mechanism of inclusion appears to involve complex interactions between TMA and HBT molecules that occur during the templating synthesis of FAU nanocrystals.

Owing to the very small size of the discrete zeolite crystals into the colloidal solution, and the reasonable concentration of HBT incorporated into FAU, we were able to carry out femtosecond pump−probe experiments and characterized the femtochemistry of HBT molecule in the zeolite host. We found that HBT upon UV excitation undergoes very fast proton transfer to solvent. This study shows that the HBT primary reactive step is not strongly influenced by the zeolite framework. This finding is promising for the development of host/guest ultrafast switching system since it reveals that on a picosecond time scale a functional guest molecule may behave in a zeolite host like in free solution. This work demonstrates, with HBT as example, the powerful alternative that represents colloidal solutions for developing host/guest systems with medium-size organic molecule where the in situ investigations of ultrafast photochemical processes are possible. The combination of nanosized porous hosts containing organic compounds such as dyes or photochromic molecules and ultrafast spectroscopy opens new perspectives for the development of molecular size devices. It is also shown that the time-resolution of the pump−probe system is not degraded using colloidal solutions containing nanosized zeolites.

Acknowledgment. This research was supported by a Marie Curie Fellowship of the European Community program (HPMFCT-2000-00684), DFG-CNRS, and BFHZ.

Note Added after ASAP Posting. This paper was posted ASAP on November 9, 2004, without all corrections. The corrections are throughout the text and include a revised Figure 8 and a new reference (no. 55). The corrected paper was posted November 15, 2004.

References and Notes

(1) Pauchard, M.; Devaux, A.; Calzaferri, G. *Chem.−Eur. J.* **2000**, *6*, 3456.
(2) Bein, T. *Chem. Mater.* **1996**, *8*, 1636.
(3) Vietze, U.; Krauss, O.; Laeri, F.; Ihlein, G.; Schüth, F.; Limburg, B.; Abraham, M. *Phys. Rev. Lett.* **1998**, *81*, 4628.
(4) Ozin, G. A.; Kuperman, A.; Stein, A. *Angew. Chem.* **1989**, *101*, 373.
(5) Nunoz, B.; Ramila, A.; Perez-Pariente, J.; Diaz, I.; Vallet-Regi, M. *Chem. Mater.* **2003**, *15*, 500.
(6) Xia, Y.; Gates, B.; Yin, Y.; Lu, Y. *Adv. Mater.* **2000**, *12*, 693.
(7) Iler, R. K. *The Chemistry of Silica*; Wiley-Interscience: New York, 1979.
(8) Ueda, M.; Kudo, K.; Ichimura, K. *J. Mater. Chem.* **1995**, *5*, 1007.
(9) Wirnsberger, G.; Scott, B. J.; Chmelka, B. F.; Stucky, G. D. *Adv. Mater.* **2000**, *12*, 1450.
(10) Casades, I.; Constantine, S.; Cardin, D.; Garrcia, H.; Gilbert, A.; Marquez, F. *Tetrahedron* **2000**, *56*, 6951.
(11) Das, K.; Sarkar, N.; Das, S.; Datta, A.; Bhattacharyya, K. *Chem. Phys. Lett.* **1996**, *249*, 323.
(12) Uppili, S.; Thomas, K. J.; Crompton, E. M.; Ramamurthy. *Langmuir* **2000**, *16*, 265.
(13) Alvaro, M.; Chretien, M. N.; Ferrer, B.; Fornes, V.; Garcia, H.; Scaiano, J. C. *Chem. Commun.* **2001**, 2106.
(14) Megelski, S.; Lieb, A.; Pauchard, M.; Drechsler, A.; Glaus, S.; Debus, Ch.; Meixner, A. J.; Calzaferri, G. *J. Phys. Chem. B.* **2001**, *105*, 25.
(15) Hoffmann, K.; Marlow, F.; Caro, J. *Adv. Mater.* **1997**, *9*, 567.

(16) Wark, M.; Ganschow, M.; Rohlfing, Y.; Schulz-Ekloff, G.; Woehrle, D. Zeolites and Mesoporous Materials at the Dawn of the 21st Century. *Stud. Surf. Sci. Catal.* **2001**, *135*, 3292.
(17) Wöhrle, D.; Schulz-Ekloff, G. *Adv. Mater.* **1994**, *6*, 875.
(18) Corrent, S.; Cosa, G.; Scaiano, J. C.; Galletero, M. S.; Alvaro, M.; Garcia, H. *Chem. Mater.* **2001**, *13*, 715.
(19) Cundy, C. S., Cox, P. A. *Chem. Rev.* **2003**, *103*, 663.
(20) Mintova, S.; Olson, N.; Valtchev, V.; Bein, T. *Science* **1999**, *283*, 958.
(21) Kirschhock, C. E. A.; Buschmann, V.; Kremer, S.; Ravishankar, R.; Houssin, C. J. Y.; Mojet, B. L.; van Santen, R. A.; Grobet, P. J.; Jacobs, P. A.; Martens, J. A. *Angew. Chem. Int. Ed. Engl.* **2001**, *40*, 2637.
(22) Yin, Y.; Lu, Y.; Gates, B.; Xia, Y. J. *Am. Chem. Soc.* **2001**, *123*, 8718.
(23) Gener, I.; Buntinx, G.; Moissette, A.; Bremard, C. *J. Phys. Chem. B* **2002**, *106*, 10322.
(24) Moya-Barrios, R.; Cozens, F. L. *Org. Lett.* **2004**, in press.
(25) Kortüm, G. *Reflectance Spectroscopy*; Springer-Verlag: New York, 1969.
(26) Bonn, M.; Bakker, H. J.; Domen, K.; Hirose, C.; Kleyn, A. W.; Van Santen, R. A. *Catal. Rev.-Sci. Eng.* **1998**, *40*, 127.
(27) Onda, K.; Yaginuma, M.; Yokota, T.; Wada, A.; Domen, K.; Hirose, C.; Kano, S. *J. Chem. Phys.* **1998**, *108*, 5935.
(28) Rurack, K.; Hoffmann, K.; Al-Soufi, W.; Resch-Genger, U. *J. Phys. Chem. B* **2002**, *106*, 9744.
(29) Flachenecker, G.; Ermoshin, V. A.; Engel, V.; Neder, R.; Wirnsberger, G.; Materny, A. *Phys. Chem. Chem. Phys.* **2003**, *5*, 865.
(30) Castagnola, N. B.; Dutta, P. *J. Phys. Chem. B* **2001**, *105*, 1537.
(31) Brewer, W. E.; Martinez, M. L.; Chou, P.-T. *J. Phys. Chem.* **1990**, *94*, 1915.
(32) Laermer, F.; Elsaesser, T.; Kaiser, W. *Chem. Phys. Lett.* **1988**, *148*, 119.
(33) Lochbrunner, S.; Wurzer, A. J.; Riedle, E. *J. Phys. Chem. A* **2003**, *107*, 10580.
(34) Lochbrunner, S.; Stock, K.; de Waele, V.; Riedle, E. *Femtochemistry and Femtobiology: Ultrafast Dynamics in Molecular Science*; Douhal, A., Santamaria, J., Eds.; World Scientific Publishing House: River Edge, NJ, 2002; p 202.
(35) Elsaesser, T.; Schmetzer, B. *Chem. Phys. Lett.* **1987**, *140*, 293.
(36) Woolfe, G. J.; Melzig, M.; Schneider, S.; Dörr, F. *Chem. Phys.* **1983**, *77*, 213.
(37) Nakagi, R.; Kobayashi, T.; Nagakura, S. *Bull. Chem. Soc. Jpn.* **1978**, *51*, 1671.
(38) Stein, M.; Keck, J.; Waiblinger, F.; Kramer, H. E. A.; Hartschuh, A.; Port, H.; Leppard, D.; Rytz, G. *J. Phys. Chem. A* **2002**, *106*, 2055.
(39) Krishnamurthy, M.; Dogra, S. *J. Photochemistry* **1986**, *32*, 235.
(40) Mosquera, M.; Penedo, J. C.; Rios Rodrigues, M. C.; Rodriguez-Prieto, F. R. J. *J. Phys. Chem.* **1996**, *100*, 5398.
(41) Potter, C. A. S.; Brown, R. G. *Chem. Phys. Lett.* **1988**, *153*, 7.
(42) Kubo, Y.; Maeda, S.; Tokita, S.; Kubo, M. *Nature* **1996**, *382*, 522.
(43) Hong, S. B. *Micropor. Mater.* **1995**, *4*, 309.
(44) Dutta, P. K.; Del Barco, B.; Shieh, D. C. *Chem. Phys. Lett.* **1986**, *127*, 200.
(45) Brenard, C.; Le Maire, M. *J. Phys. Chem.* **1993**, *97*, 9695.
(46) Krause, K.; Geidel, E.; Kindler, J.; Förster, H.; Böhling, H. *Chem. Commun.* **1995**, 2481.
(47) Bornhauser, P.; Bougeard, D. *J. Raman Spectrosc.* **2001**, *32*, 279.
(48) Sharma, S. K.; Mammone, J. F.; Nicol, M. F. *Nature* **1981**, *292*, 140.
(49) Dowty, E. *Phys. Chem. Miner.* **1987**, *14*, 122.
(50) Jarman, R. H.; Melchior, M. T. *J. Chem. Soc. Chem. Commun.* **1984**, 414.
(51) (a) Fisher, T. H.; Chao, P.; Upton, C. G.; Day, A. J. *Magn. Reson. Chem.* **2000**, *40*, 747. (b) http://www.aist.go.jp/RIODB/SDBS/menu-e.html; SDBS No: 554.
(52) (a) Wang, W.; De Cola, P. L.; Glaeser, R.; Ivanova, I. I.; Weitkamp, J.; Hunger, M. *Catal. Lett.* **2004**, *94*, 119. (b) http://www.aist.go.jp/RIODB/SDBS/menu-e.html; SDBS No: 1154.
(53) Paterson, M. J.; Robb, M. A.; Blancafort, L.; DeBellis, A. D. *J. Am. Chem. Soc.* **2004**, *126*, 2912.
(54) Poizat, O., Bardez, E.; Buntinx, G.; Alain, V. *J. Chem. Phys.* **2004**, *108*, 1873.
(55) Lorenc, M.; Ziolek, M.; Naskrecki, R.; Karolczak, J.; Kubicki, J.; Maciejewski, A. *Appl. Phys. B* **2002**, *74*, 19.